

Room temperature ferroic orders in Zr and (Zr, Ni) doped SrTiO₃

Shahran Ahmed,¹ A. K. M. Sarwar Hossain Faysal,¹ M. N. I. Khan,^{2,*} M. A. Basith,^{3,†}
Muhammad Shahriar Bashar,⁴ H. N. Das,² Tarique Hasan,¹ and Imtiaz Ahmed^{1,‡}

¹*Department of Electrical and Electronic Engineering, University of Dhaka, Dhaka-1000, Bangladesh*

²*Materials Science Division, Atomic Energy Centre, Dhaka-1000, Bangladesh*

³*Nanotechnology Research Laboratory, Department of Physics,*

Bangladesh University of Engineering and Technology, Dhaka-1000, Bangladesh

⁴*Institute of Fuel Research and Development, Bangladesh Council of Scientific and Industrial Research, Dhaka-1205, Bangladesh*

We synthesized strontium titanate SrTiO₃ (STO), Zr doped Sr_{1-x}Zr_xTiO₃ and (Zr, Ni) co-doped Sr_{1-x}Zr_xTi_{1-y}Ni_yO₃ samples using solid state reaction technique to report their structural, electrical and magnetic properties. The cubic *Pm-3m* phase of the synthesized samples has been confirmed using Rietveld analysis of the powder X-ray diffraction pattern. The grain size of the synthesized materials was reduced significantly due to Zr doping as well as (Zr, Ni) co-doping in STO. The chemical species of the samples were identified using energy-dispersive X-ray spectroscopy. We observed forbidden first order Raman scattering at 148, 547 and 797 cm⁻¹ which may indicate nominal loss of inversion symmetry in cubic STO. The absence of absorption at 500 cm⁻¹ and within 600-700 cm⁻¹ band in Fourier Transform Infrared spectra corroborates Zr and Ni as substitutional dopants in our samples. Due to 4% Zr doping in Sr_{0.96}Zr_{0.04}TiO₃ sample dielectric constant, remnant electric polarization, remnant magnetization and coercivity were increased. Notably, in the case of 4% Zr and 10% Ni co-doping we have observed clearly the existence of both FE and FM hysteresis loops in Sr_{0.96}Zr_{0.04}Ti_{0.90}Ni_{0.10}O₃ sample. In this co-doped sample, the remnant magnetization and coercivity were increased by ~1 and ~2 orders of magnitude respectively as compared to those of undoped STO. The coexistence of FE and FM orders in (Zr, Ni) co-doped STO might have the potential for interesting multiferroic applications.

I. INTRODUCTION

Strontium titanate SrTiO₃ (STO) is perhaps one of the most prominent prototypical ABO₃ perovskite oxide materials having potentials in diverse fields of applications such as high-k dielectrics [1], substrate materials [2], tunable microwave devices [3, 4], non-volatile memory applications [5], O₂ and H₂S sensing [6, 7] and photocatalytic water splitting [8], to name just a few. At room temperature, STO exists in cubic structure with space group *Pm-3m* where the Sr²⁺ occupies A site which is surrounded by four TiO₆ octahedra and Ti⁴⁺ occupies B site which is located at the octahedral void formed by six O²⁻ ions situated at the faces of the cube [9]. Pure stoichiometric STO is a band-insulator whose quantum paraelectric behaviour excludes the emergence of the ferroic phases such as ferroelectric (FE) and ferromagnetic (FM) orders [10–14]. Over the years numerous attempts have been made to induce FE and FM orders in STO by means of cation doping for achieving multiferroic behaviour. The FM ordering is induced in STO by doping transition metals (Mn, Fe, Co, Cd) and rare-earth elements (Yb, Mn)[15–20]. The FE behavior has been observed at room temperature in Pr doped STO [21] whereas Mn doping introduced FE relaxor type behaviour at low temperature [14, 22–25]. Moreover, (Nd, Dy) and (La, Mn) co-doped STO showed promising results for multiferroic applica-

tions [14, 21–25].

Here we doped STO with two different transition metal elements which are Zr and Ni. In the stable Zr⁴⁺ oxidation state, the empty 4d orbital has the possibility of inducing the ferroelectric order in STO and thereby may enhance dielectric properties in Zr doped STO [10, 26, 27]. The rationale behind co-doping of Zr⁴⁺ and Ni²⁺ is that the magnetic moments of the unpaired electrons in the partially filled 3d orbitals in Ni²⁺ oxidation state might have the potential to tune the magnetic properties of STO. We assume substitutional doping following the general rule where ions with smaller radius Ni²⁺ ($r_o = 0.69$ Å) tend to substitute Ti⁴⁺ in B site and ions with larger radius Zr⁴⁺ ($r_o = 0.80$ Å) prefer to go in A site occupied by Sr²⁺ [28]. The objective of this investigation is to synthesize a number of Zr and Ni co-doped STO materials and extensively characterize their structural, electrical and magnetic properties [29–32]. To this aim, undoped STO, Zr-doped Sr_{1-x}Zr_xTiO₃ and (Zr, Ni) co-doped Sr_{1-x}Zr_xTi_{1-y}Ni_yO₃ samples were synthesized using solid state reaction technique. Based on the findings from the pertinent materials characterization techniques, we report a particular composition of this (Zr, Ni) co-doped samples with improved multiferroic properties which might have potential for multifunctional applications [30].

* ni_khan77@yahoo.com

† mabasith@phy.buet.ac.bd

‡ imtiaz@du.ac.bd

II. METHODOLOGY

A. Sample Preparation

A number of samples for undoped SrTiO_3 , Zr-doped SrTiO_3 and (Zr, Ni) co-doped SrTiO_3 have been synthesized using the standard solid state reaction method [33, 34]. For the starting materials, proper combinations of analytical grade SrCO_3 (98% pure), TiO_2 (99.9% pure), ZrO_2 (99.9% pure) and NiO (99.9% pure) were used with desired stoichiometric ratio. For the Zr-doped samples, $x = 0.02, 0.04, 0.06$ were prepared with the chemical formula $\text{Sr}_{1-x}\text{Zr}_x\text{TiO}_3$. In case of (Zr, Ni) co-doped samples with chemical formula $\text{Sr}_{1-x}\text{Zr}_x\text{Ti}_{1-y}\text{Ni}_y\text{O}_3$, a series of combinations with $y = 0.05, 0.10, 0.15$ and 0.20 for fixed $x = 0.04$ have been synthesized. The powder mixtures were hand milled for 6 hours using mortar and pestle to produce a homogeneous solid mixture with fine constituent particles in proximity with each other. Several droplets of polyvinyl alcohol were mixed with the samples in a steel die to facilitate binding before being subjected to uniaxial force of 20 kN in a hydraulic press to form circular disk-shaped pellets. These pellets were calcined at 800°C for 4 hours to promote reaction among the mixture constituents. The pre-sintered disk-shaped pellets were smashed into fine powders by hand milling in a ceramic mortar and pestle for 3 hours to expedite solid state reactions probabilities in the subsequent sintering of the samples. The crystallization temperatures of the undoped, Zr doped and (Zr, Ni) co-doped samples were measured to be $\sim 1080^\circ$, $\sim 1085^\circ$ and $\sim 942^\circ\text{C}$ respectively using a differential scanning calorimeter. The pre-sintered powder materials were pressed into circular disk shaped pellets and toroid rings by using a hydraulic press and sintered at 1250°C for 4 hours.

B. Characterization Techniques

To estimate the crystallization temperature of our synthesized samples, the differential scanning calorimetry was performed using a NETZSCH STA 449 F3 Jupiter simultaneous thermal analyzer. The high temperature sintering of the samples was done in a Nabertherm Muffle Furnace LT 5/14. The X-ray Diffraction (XRD) patterns for the synthesized samples were obtained from 10° to 80° at 35 kV accelerating voltage with an emission current of 20 mA using a Rigaku SmartLab SE multipurpose XRD system with $\text{Cu K}\alpha$ radiation ($\lambda = 0.15418\text{ nm}$). The surface morphology and chemical species identification were performed with Scanning Electron Microscopy (SEM) and Energy-dispersive X-ray spectroscopy (EDX) respectively using a AVO 18 Research Scanning Electron Microscope from ZEISS. The room temperature Raman scattering spectroscopy was performed with a Confocal Raman Microscope MonoVista CRS+ using a 532.090 nm laser. To characterize the chemical bond vibrations inside our samples, we used the KBr pellet technique in Fourier

Transform Infrared (FTIR) PerkinElmer Spectrum spectrometer. The dielectric constant and resistivity of the samples were measured from complex impedance spectroscopy performed by Wayne Kerr 6500B Impedance Analyzer. For the electric hysteresis measurements, the electric polarization P vs electric field E loops were recorded using a Precision Multiferroic II Ferroelectric Test System from Marine India. The magnetization M vs. magnetic field H hysteresis loops of the samples were obtained using a vibrating sample magnetometer VSM from Quantum Design PPMS DynaCool.

III. RESULTS AND DISCUSSION

A. X-ray Diffraction Analysis

We have investigated the crystallographic structure, phase and purity of the synthesized samples using the XRD patterns, see Fig. 1. The pure STO exhibit cubic $Pm-3m$ phase (space group no. 221) according to the standard JCPDS data (01-084-0443) [17, 35]. The phase purity and crystalline nature of the samples were evident from the sharp and intense diffraction peaks. In case of Zr doped $\text{Sr}_{1-x}\text{Zr}_x\text{TiO}_3$ samples, extraneous peaks started to appear for $x = 0.06$ indicating the presence of additional phases on top of the cubic phase. Hence, to avoid the influence of these secondary phases in (Zr, Ni) co-doped samples, we fixed Zr concentration x to be at 0.04 as $\text{Sr}_{0.96}\text{Zr}_{0.04}\text{Ti}_{1-y}\text{Ni}_y\text{O}_3$. For $y \geq 0.10$, the small extraneous peaks at 37.18° , 43.20° , 62.75° and 75.25° were observed due to excess NiO [36]. The lattice parameters were extracted by Rietveld refinement of the XRD profile using FullProf software. We estimated bulk density, X-ray density, porosity, crystallite size and full-width-half-maximum using standard techniques [37], see Table I. The bulk density remained unchanged for undoped and doped STO. For Zr doped and (Zr, Ni) co-doped samples, an increasing trend in the X-ray-density was observed with Zr and Ni concentrations. These increments may have originated from the change in molecular weights due to the incorporation of the Zr and Ni dopants in the sample. A nominal variation in porosity has been observed across the synthesized samples. As for the crystallite size, monotonic decrements have been detected with increasing Zr concentration in STO. The change in the full-width-at-half-maximum (FWHM) for (Zr, Ni) co-doped samples indicates slight distortion and disorder due to size differences of dopants and interstitial dopants respectively [38]. From the peak shift analysis (as shown in Fig. S1 of the Supplementary Information), it is evident that the peak shift between pure STO and $\text{Sr}_{0.96}\text{Zr}_{0.04}\text{TiO}_3$ is very nominal almost conforming with pure cubic phase. We superimposed the Rietveld refined pattern on experimentally measured XRD data for three selected samples; SrTiO_3 , $\text{Sr}_{0.96}\text{Zr}_{0.04}\text{TiO}_3$ (due to superior dielectric properties in Section III E) and $\text{Sr}_{0.96}\text{Zr}_{0.04}\text{Ti}_{0.90}\text{Ni}_{0.10}\text{O}_3$ (manifested superior magnetic

XRD analysis $\text{Sr}_{1-x}\text{Zr}_x\text{Ti}_{1-y}\text{Ni}_y\text{O}_3$ samples													
Composition		Lattice Parameters							Bulk Density	X-ray density	Porosity	Crystallite Size	FWHM
x	y	a(Å)	b(Å)	c(Å)	c/a	$\alpha(^{\circ})$	$\beta(^{\circ})$	$\gamma(^{\circ})$	(gcm^{-3})	(gcm^{-3})	(%)	(nm)	(110)($^{\circ}$)
0.00	0.00	3.908	3.908	3.908	1.0	90	90	90	3.99	5.102	21.7	108	0.073
0.02	0.00	3.903	3.903	3.903	1.0	90	90	90	3.99	5.127	22.1	88	0.086
0.04	0.00	3.899	3.899	3.899	1.0	90	90	90	3.99	5.145	22.4	57	0.135
0.06	0.00	3.908	3.908	3.908	1.0	90	90	90	3.99	5.109	21.8	55	0.137
0.04	0.05	3.905	3.905	3.905	1.0	90	90	90	3.99	5.133	22.2	100	0.085
0.04	0.10	3.888	3.888	3.888	1.0	90	90	90	3.99	5.218	23.5	36	0.193
0.04	0.15	3.897	3.897	3.897	1.0	90	90	90	3.99	5.169	22.8	36	0.202
0.04	0.20	3.894	3.894	3.894	1.0	90	90	90	3.99	5.195	23.1	49	0.148

TABLE I. Lattice parameters a , b , c , α , β and γ extracted from Rietveld refinement of XRD patterns of $\text{Sr}_{1-x}\text{Zr}_x\text{Ti}_{1-y}\text{Ni}_y\text{O}_3$ for $(x, y) = (0.00, 0.00)$, $(0.02, 0.00)$, $(0.04, 0.00)$, $(0.06, 0.00)$, $(0.04, 0.05)$, $(0.04, 0.10)$, $(0.04, 0.15)$ and $(0.04, 0.20)$. The bulk density, X-ray density, porosity, crystallite size were derived from standard formulas. The values for FWHM were for the most intense XRD peak corresponding to (110) plane.

properties as shall be seen later in Section III H) in Fig. 2. The goodness of fitting parameter χ^2 for the three samples were found to be 3.784, 3.590 and 3.806 which indicate simulated patterns are in good agreement with experimental observations conforming cubic structure. The auxiliary crystallographic parameters such as atomic positions in Wyckoff coordinates, relevant bond lengths and bond angles have also been extracted from the refinement (see Table S1 in the Supplementary Information).

B. Morphological and EDX Analysis

To understand the effect of doping on the microstructure and to perform chemical species identification of our samples, SEM micrographs and EDX spectra of the three selected samples SrTiO_3 , $\text{Sr}_{0.96}\text{Zr}_{0.04}\text{TiO}_3$ and $\text{Sr}_{0.96}\text{Zr}_{0.04}\text{Ti}_{0.90}\text{Ni}_{0.10}\text{O}_3$ have been obtained. The average grain size was estimated to be $2 \mu\text{m}$ in case of undoped SrTiO_3 , see SEM micrograph in Fig. 3(a). The estimated average grain size is comparable with the previous studies on STO in Refs. [28, 39]. The detection of Sr, Ti and O peaks in the corresponding EDX spectra for undoped STO excludes the presence of unwanted chemical species in the sample (see Fig. S2(a) in the Supplementary Information). The average grain size was reduced to $0.343 \mu\text{m}$ for $\text{Sr}_{0.96}\text{Zr}_{0.04}\text{TiO}_3$ sample as showed in Fig. 3(b). This shrinkage of the gain size can be due to the presence of Zr or Ti at the grain boundaries [28]. In addition, Zr substitution prompted grain irregularity and inhomogeneity. The presence of Zr peak in addition with Sr, Ti and O peaks in the corresponding EDX spectra for $\text{Sr}_{0.96}\text{Zr}_{0.04}\text{TiO}_3$ corroborates its incorporation as a dopant in the sample (see Fig. S2(b) in the Supplementary Information). For (Zr, Ni) co-doped $\text{Sr}_{0.96}\text{Zr}_{0.04}\text{Ti}_{0.90}\text{Ni}_{0.10}\text{O}_3$ sample, the estimated grain size was found to be $0.341 \mu\text{m}$ according to the SEM micrograph in Fig. 3(c). The corresponding EDX spectra containing Zr and Ni peaks elucidates the co-doping of the STO (see Fig. S2(c) in the Supplementary Information). Moreover the atomic weights (%) of

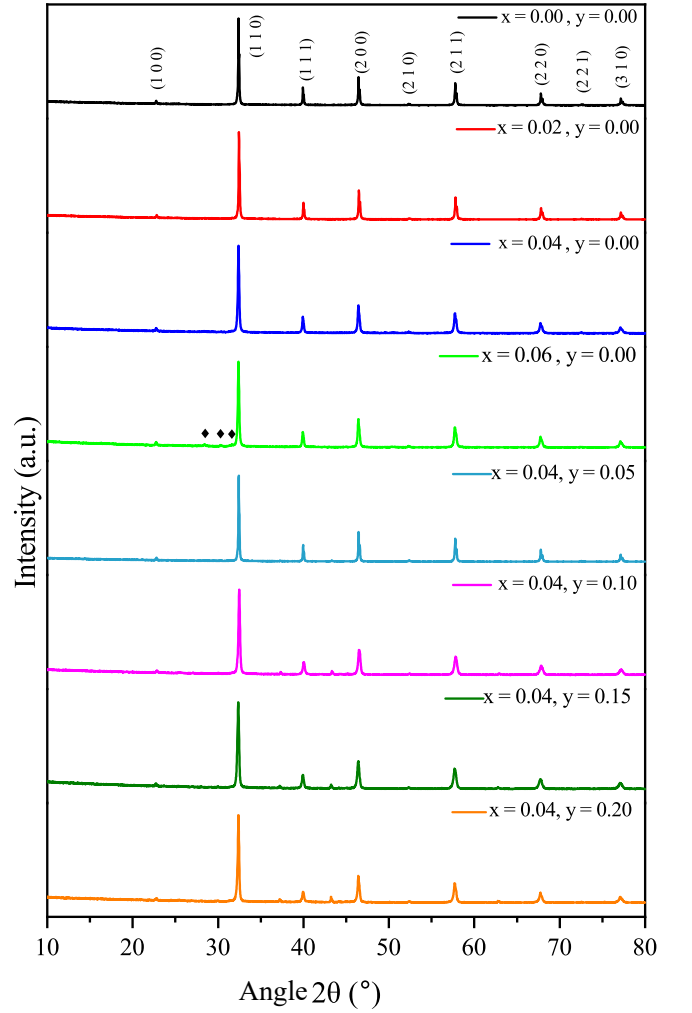


FIG. 1. X-ray diffraction patterns of $\text{Sr}_{1-x}\text{Zr}_x\text{Ti}_{1-y}\text{Ni}_y\text{O}_3$ for $(x, y) = (0.00, 0.00)$, $(0.02, 0.00)$, $(0.04, 0.00)$, $(0.06, 0.00)$, $(0.04, 0.05)$, $(0.04, 0.10)$, $(0.04, 0.15)$ and $(0.04, 0.20)$. The unknown impurity phase is marked with black diamonds in case of $(x, y) = (0.06, 0.00)$.

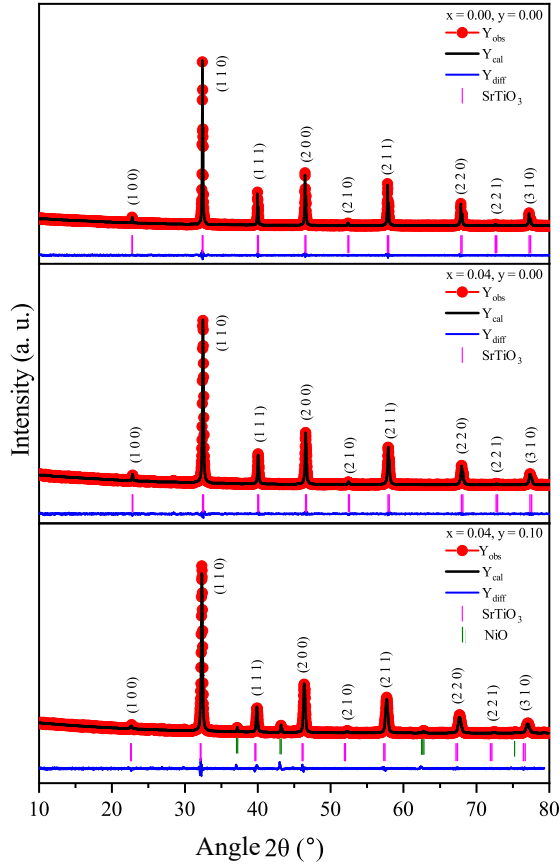


FIG. 2. Simulated Rietveld least square minimized XRD patterns superimposed on experimentally observed data of $\text{Sr}_{1-x}\text{Zr}_x\text{Ti}_{1-y}\text{Ni}_y\text{O}_3$ for $(x,y) = (0.00, 0.00)$, $(0.04, 0.00)$ and $(0.04, 0.10)$. The red solid circles are the experimental data points (Y_{obs}), the dark solid line represents calculated refined pattern Y_{cal} , the bottom blue curve Y_{diff} shows difference between the experimental Y_{obs} and calculated Y_{cal} values and pink vertical lines mark the positions of Bragg peaks for cubic SrTiO_3 with $Pm-3m$ space group. The green vertical lines represent NiO phase.

chemical species in all aforementioned samples were compared with the corresponding theoretical values in Table S2 of the Supplementary Information.

C. Raman Analysis

We performed room temperature Raman scattering spectroscopy to characterize the vibrational phonon in terms of transverse acoustic (TA), longitudinal acoustic (LA), transverse optical (TO) and longitudinal optical (LO) modes of our samples. For a three dimensional ($d = 3$) unit cell with cubic symmetry, the STO contains $n = 5$ atoms (one Sr, one Ti and three O) that generates $3n = 15$ vibrational phonon modes; out of which the 3 low frequency acoustic modes (F_{1u}) are degenerate, 3 degenerate optical modes (F_{1u}) are Raman and infrared

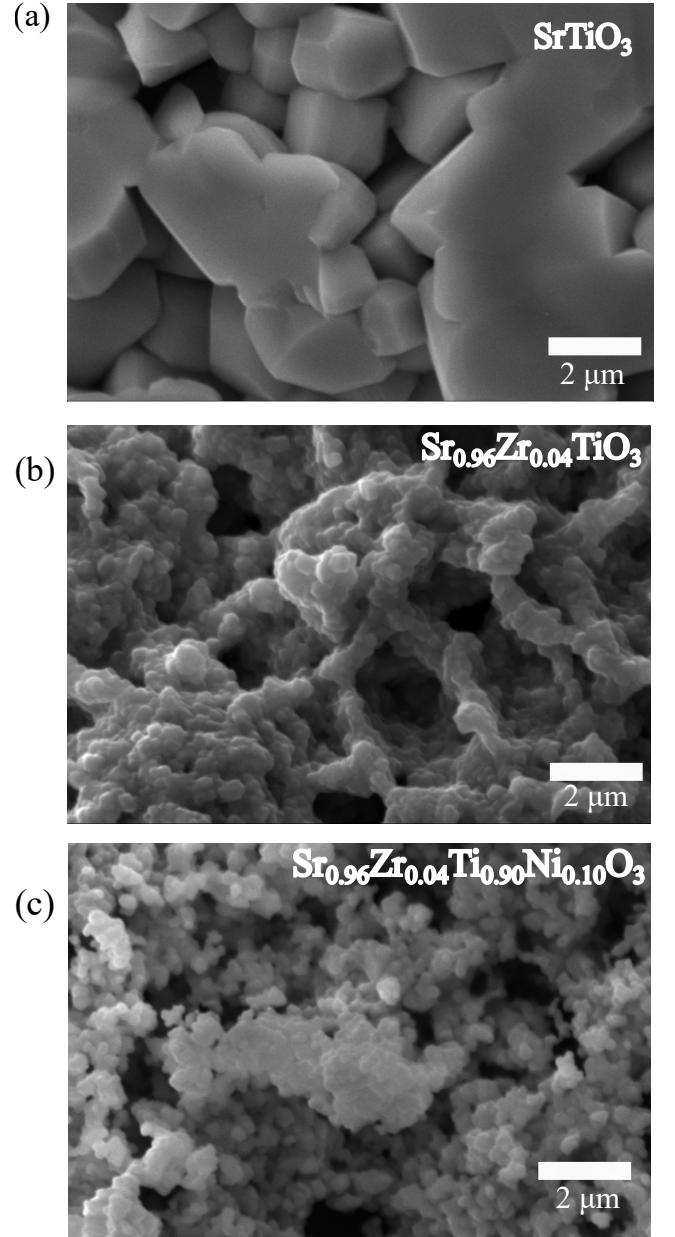


FIG. 3. SEM micrographs (a) SrTiO_3 , (b) $\text{Sr}_{0.96}\text{Zr}_{0.04}\text{TiO}_3$ and (c) $\text{Sr}_{0.96}\text{Zr}_{0.04}\text{Ti}_{0.90}\text{Ni}_{0.10}\text{O}_3$ samples.

(IR) inactive and the rest of 9 optical modes (F_{2u}) are IR-active [40–44]. As cubic symmetry forbids first order Raman scattering, the Raman modes in cubic STO originate from second order scattering processes [40]. The two photon momentum conservation processes made the second order Raman scattering peaks to appear broad and continuous, see Fig. 4. The broad intensity peaks of the Raman scattered radiation appeared in $250\text{--}500\text{ cm}^{-1}$ and $600\text{--}800\text{ cm}^{-1}$ wave number ranges. These Raman peaks were identified with corresponding vibrational phonon modes of the samples according to Refs. [42, 43] in Table S3 of the Supplementary Information. The 2TA

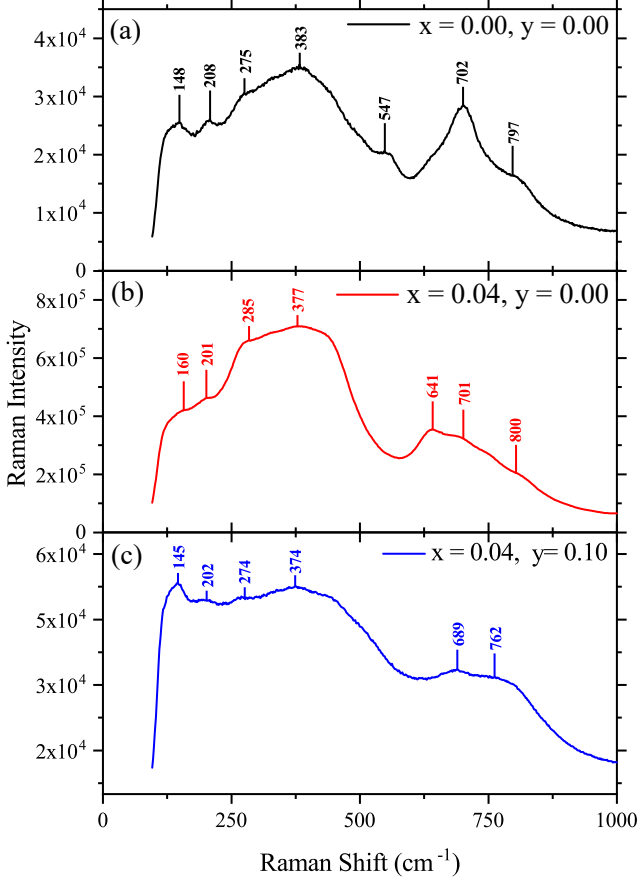


FIG. 4. Raman spectra of (a) SrTiO_3 , (b) $\text{Sr}_{0.96}\text{Zr}_{0.04}\text{TiO}_3$ and (c) $\text{Sr}_{0.96}\text{Zr}_{0.04}\text{Ti}_{0.90}\text{Ni}_{0.10}\text{O}_3$ samples.

mode appeared around 208 cm^{-1} , whereas the combined acoustic and optical modes such as TO_1+LA , LO_1+TA and $\text{LA}+\text{LO}_3$ contributed at 275 , 383 and 702 cm^{-1} respectively. The modes corresponding to two optical phonons such as TO_1+TO_4 (641 cm^{-1}) and LO_3+TO_2 (762 cm^{-1}) were there for both Zr and (Zr, Ni) co-doped STO. The presence of peaks at 148 cm^{-1} (TO_1), 547 cm^{-1} (TO_4) and 797 cm^{-1} (LO_4) for undoped STO can be attributed to forbidden first order Raman scattering. This may indicate a nominal loss of inversion symmetry due to surface frozen dipoles and oxygen vacancies [45, 46]. In case of doped samples, this nominal symmetry breaking can happen due to incorporation of dopants in the host STO [18].

D. Fourier Transform Infrared Spectroscopy

We also measured FTIR spectra for the undoped STO, 4% Zr doped $\text{Sr}_{0.96}\text{Zr}_{0.04}\text{TiO}_3$ and (4% Zr, 10% Ni) co-doped $\text{Sr}_{0.96}\text{Zr}_{0.04}\text{Ti}_{0.90}\text{Ni}_{0.10}\text{O}_3$ samples at room temperature from 350 to 4000 cm^{-1} and displayed in Fig. 5. The measured FTIR absorption peaks were identified to

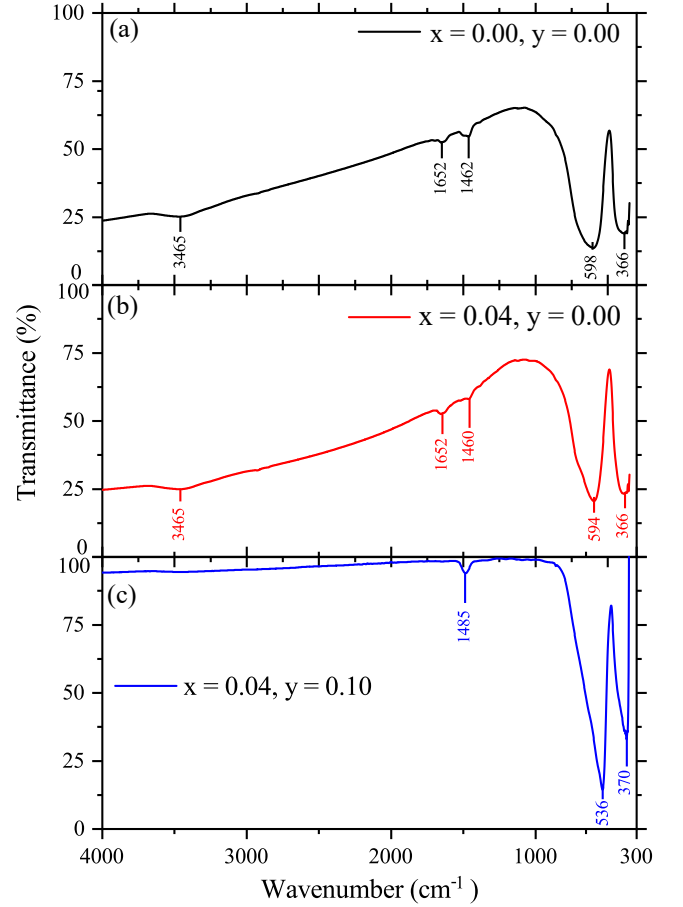


FIG. 5. FTIR spectra of (a) SrTiO_3 , (b) $\text{Sr}_{0.96}\text{Zr}_{0.04}\text{TiO}_3$ and (c) $\text{Sr}_{0.96}\text{Zr}_{0.04}\text{Ti}_{0.90}\text{Ni}_{0.10}\text{O}_3$ samples.

corresponding chemical bond vibrations following Refs. [47–50] in Table S4 of the Supplementary Information. The absorption peaks at 1652 cm^{-1} and 3465 cm^{-1} can be designated to hydroxyl $-\text{OH}$ stretching vibration, see Fig. 5 (a)&(b). The stemming of H_2O or $-\text{OH}$ in our sample may imply adsorption of water molecules from air surrounding the sample. The FTIR peaks at 1462 , 1460 and 1485 cm^{-1} for the three samples hinted deformed $-\text{OH}$ in $\text{C}-\text{OH}$ bond [47]. The trace of C may have its origin in SrCO_3 even after the calcination process. The FTIR bands in $300\text{--}600\text{ cm}^{-1}$ represent characteristic IR absorptions due to $\text{Ti}-\text{O}$ in STO. The peaks around $\sim 366\text{ cm}^{-1}$ for different samples can appear from TiO_2 bending vibrations. Moreover the one near $\sim 598\text{ cm}^{-1}$ can be ascribed to TiO_6 stretching vibration connected to Sr. We have not observed any sharp absorption peak at 500 cm^{-1} in $\text{Sr}_{0.96}\text{Zr}_{0.04}\text{TiO}_3$ which corresponds to $\text{Zr}-\text{O}$ stretching vibrations in ZrO_2 , see Fig. 5(b). This corroborates the fact that Zr^{4+} ions have been incorporated in STO lattice. But Zr^{4+} ions, as it replaces Sr^{2+} , shorten different $\text{Ti}-\text{O}$ bond lengths to different degrees; effectively generate several very closely spaced IR absorption peaks. The combined effect of these peaks is to widen

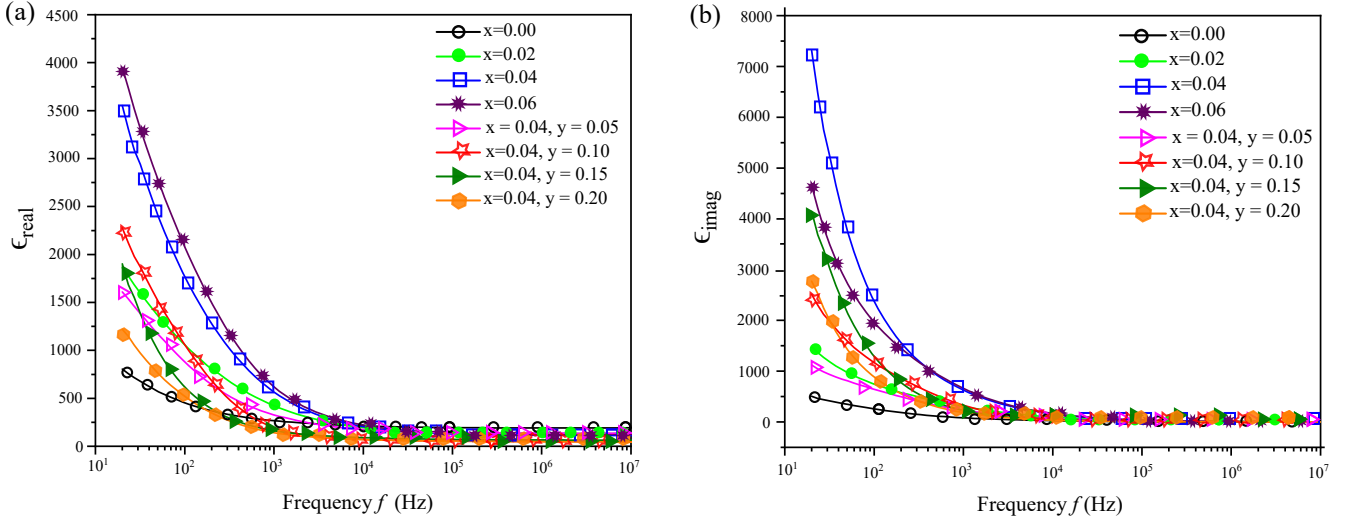


FIG. 6. (a) The real ϵ_{real} vs frequency f and (b) the imaginary part ϵ_{imag} vs frequency f of the complex dielectric constant $\epsilon = \epsilon_{\text{real}} + i\epsilon_{\text{imag}}$ of $\text{Sr}_{1-x}\text{Zr}_x\text{Ti}_{1-y}\text{Ni}_y\text{O}_3$ for $(x, y) = (0.00, 0.00)$, $(0.02, 0.00)$, $(0.04, 0.00)$, $(0.06, 0.00)$, $(0.04, 0.05)$, $(0.04, 0.10)$, $(0.04, 0.15)$ and $(0.04, 0.20)$.

the Sr–Ti–O absorption peak at 594 cm^{-1} . In case of (Zr, Ni) co-doped sample, as Ni^{2+} ions replace the Ti^{4+} , they affect Ti–O bonds and shift the Sr–Ti–O absorption peak to 536 cm^{-1} in Fig. 5(c).

E. Dielectric Measurements

The circular disk-shaped pellets were used to form parallel plate capacitors with a geometric capacitance C_0 giving rise to a frequency f and complex dielectric constant $\epsilon = \epsilon_{\text{real}} + i\epsilon_{\text{imag}}$ ($i = \sqrt{-1}$) dependent impedance $Z(f) = 1/i2\pi fC_0\epsilon$ which was measured with the impedance analyzer [51, 52]. The real part ϵ_{real} of the complex dielectric constant was plotted for $\text{Sr}_{1-x}\text{Zr}_x\text{Ti}_{1-y}\text{Ni}_y\text{O}_3$ samples as a function of excitation frequency f in Fig. 6(a). The ϵ_{real} gradually decreases with increasing f for undoped, Zr doped and (Zr, Ni) co-doped STO samples. This indicates electric dipoles inside the material struggle to synchronize and fall out of steps with high frequency electric field. The dielectric behaviour is controlled by different constituents polarizations arising from interfacial charge, space charge, oriental dipolar, ionic and electronic contributions [53]. Owing to the fact that the ϵ_{real} decays rapidly beyond 1 kHz, we attribute this to interfacial and space charge polarization effects [35, 54, 55]. This polarization may arise due to charges trapped at the interface between the sample and the electrodes, space charges at the grain boundaries, interstitial and voids. These trapped charges are sluggish in responding to the applied field in the high frequency regime beyond 1 kHz and usually modelled within the general framework of Maxwell-Wagner relaxation processes occurring inside the sample [56]. For the

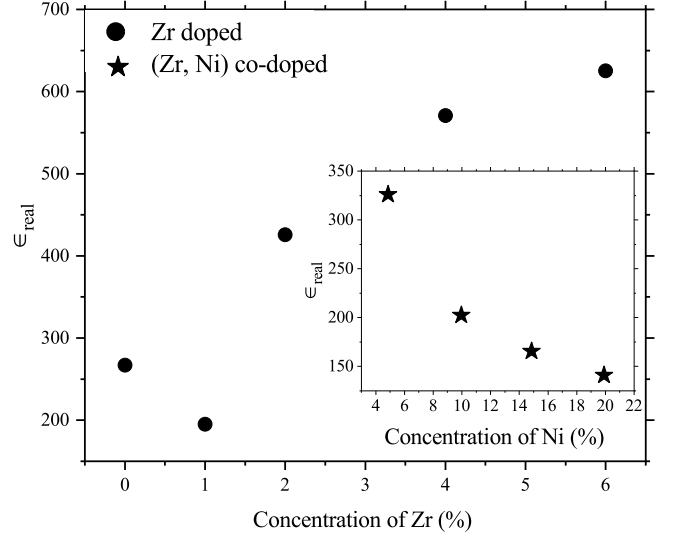


FIG. 7. The ϵ_{real} of $\text{Sr}_{1-x}\text{Zr}_x\text{TiO}_3$ sample for $x = 0.00, 0.02, 0.04$ and 0.06 . Inset: The ϵ_{real} of $\text{Sr}_{0.96}\text{Zr}_{0.04}\text{Ti}_{1-y}\text{Ni}_y\text{O}_3$ sample for $y = 0.05, 0.10, 0.15$ and 0.20 . All estimations were done at $f = 1\text{ kHz}$.

dielectric loss analysis, the imaginary part ϵ_{imag} of the complex ϵ was plotted as a function of frequency f in Fig. 6(b). This ϵ_{imag} quantifies the energy dissipation of the electric dipoles due to random collisions or phase lag during their orientation change in response to the oscillating field. The frequency response of ϵ_{imag} has similar trend as compared to ϵ_{real} , i.e. it diminishes with increasing f for undoped, Zr doped and (Zr, Ni) co-doped samples. This is expected as higher losses occur at low

frequencies due to interfacial and space charge polarizations.

The effect of doping on ϵ_{real} was analyzed in Fig. 7 for a fixed frequency of 1 kHz. For Zr doped $\text{Sr}_{1-x}\text{Zr}_x\text{TiO}_3$ samples, the ϵ_{real} increases monotonically with increasing composition $x=0.02, 0.04$ and 0.06 . This enhancement of dielectric constant can be attributed to more space charge accumulation due to higher oxidation state of Zr^{4+} as compared to Sr^{2+} in A site of STO. But in case of $\text{Sr}_{0.96}\text{Zr}_{0.04}\text{Ti}_{1-y}\text{Ni}_y\text{O}_3$ samples, ϵ_{real} decreases steadily with increasing Ni concentrations as shown in the inset of Fig. 7. This ϵ_{real} reduction may imply depletion of space charges as Ni^{2+} substitutes Ti^{4+} ion at the B-site of STO. Moreover, the substitutional Ni^{2+} can restrain the rattling of Ti^{4+} ions in TiO_6 octahedra causing the reduction of dielectric constant [28, 57, 58].

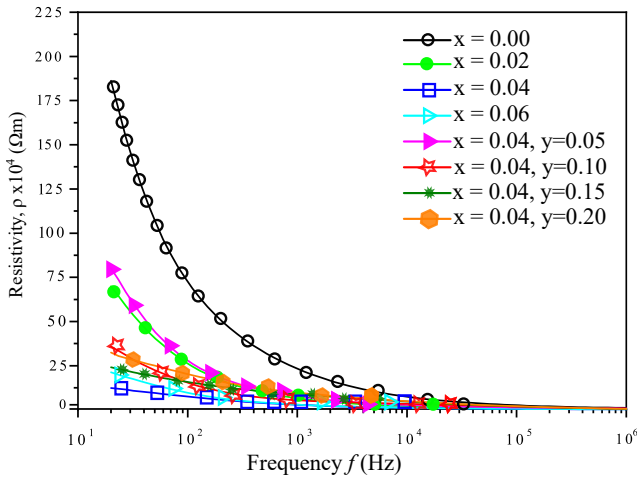


FIG. 8. The resistivity ρ of $\text{Sr}_{1-x}\text{Zr}_x\text{Ti}_{1-y}\text{Ni}_y\text{O}_3$ as a function of frequency f for $(x, y) = (0.00, 0.00), (0.02, 0.00), (0.04, 0.00), (0.06, 0.00), (0.04, 0.05), (0.04, 0.10), (0.04, 0.15)$ and $(0.04, 0.20)$.

F. Resistivity Measurements

The frequency dependant ac resistivity ρ of the samples was measured from the complex impedance $Z = Z_{\text{real}} + iZ_{\text{imag}}$ by using the relation $\rho = A_s Z_{\text{real}} / d_s$, where A_s and d_s represent area and thickness of the circular disc shape pellets respectively [59]. The resistivity ρ decays with f in Fig. 8. This indicates enhanced mobile charge hopping in the grain boundaries and sample-electrode interfaces [35, 60]. The interfacial charges can produce a thin conductive layer at the sample surface effectively reducing the resistivity at high frequencies. Moreover the carrier transport in high frequency is dominated by bulk of the grains whereas grain boundary dictates the low frequency transport [61]. The carrier activation energy at the grain boundaries may fall at high frequencies resulting in enhanced charge conduction [62]. To analyze the effect of

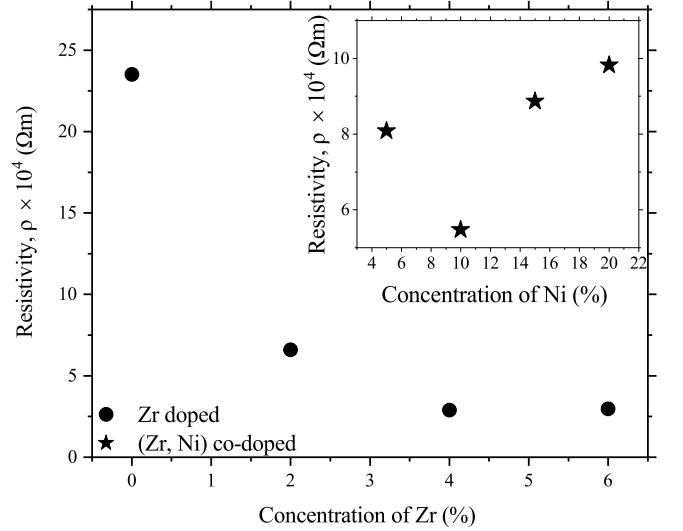


FIG. 9. The resistivity ρ at a fixed frequency $f = 1$ kHz of $\text{Sr}_{1-x}\text{Zr}_x\text{TiO}_3$ samples for $x = 0.00, 0.02, 0.04$ and 0.06 . Inset: The ρ of $\text{Sr}_{0.96}\text{Zr}_{0.04}\text{Ti}_{1-y}\text{Ni}_y\text{O}_3$ samples for $y = 0.05, 0.10, 0.15$ and 0.20 .

doping, we plot ρ for undoped, Zr doped $\text{Sr}_{1-x}\text{Zr}_x\text{TiO}_3$ and (Zr, Ni) co-doped $\text{Sr}_{0.96}\text{Zr}_{0.04}\text{Ti}_{1-y}\text{Ni}_y\text{O}_3$ samples at a fixed f of 1 kHz in Fig. 9. The insulating characteristics of undoped STO is well captured in its high resistivity value. As we dope STO with Zr, the resistivity ρ of the $\text{Sr}_{1-x}\text{Zr}_x\text{TiO}_3$ samples decreases with increasing concentrations $x = 0.02, 0.04$. This can be attributed to the fact that Zr^{4+} acts as an n-type dopant for Sr^{2+} and raises the conductivity of the samples. The Ni, as a second dopant in $\text{Sr}_{0.96}\text{Zr}_{0.04}\text{Ti}_{1-y}\text{Ni}_y\text{O}_3$ samples, seems to gradually increase the ρ for $y = 0.10, 0.15$ and 0.20 as shown in the inset of Fig. 9. A number of reasons can be ascribed to this conductivity depletion. The Ni^{2+} ion can act as an acceptor dopant for Ti^{4+} . This suppresses the n-type conductivity between the grain bulks as acceptor dopants can act as a non-conductive layer for mobile charge carriers across the grain boundaries [63, 64]. Moreover, any oxygen vacancies induced by Ni^{2+} can act as a charge trapping center reducing the carrier mobility.

G. Electric Hysteresis Measurements

The room temperature electric polarization (P) vs electric field (E) hysteresis P - E loops were measured with external triangular ac field excitation up to ± 3 kVcm^{-1} at 50 Hz for undoped, Zr doped and (Zr, Ni) co-doped samples. The standard P - E loop parameters such as coercive electric field E_c , remnant polarization P_r , maximum polarization P_{max} and leakage current I_d at P_{max} were extracted and displayed in Table II. The undoped STO exhibits a small P - E hysteresis loop where the P is almost linear with E and does not reach any

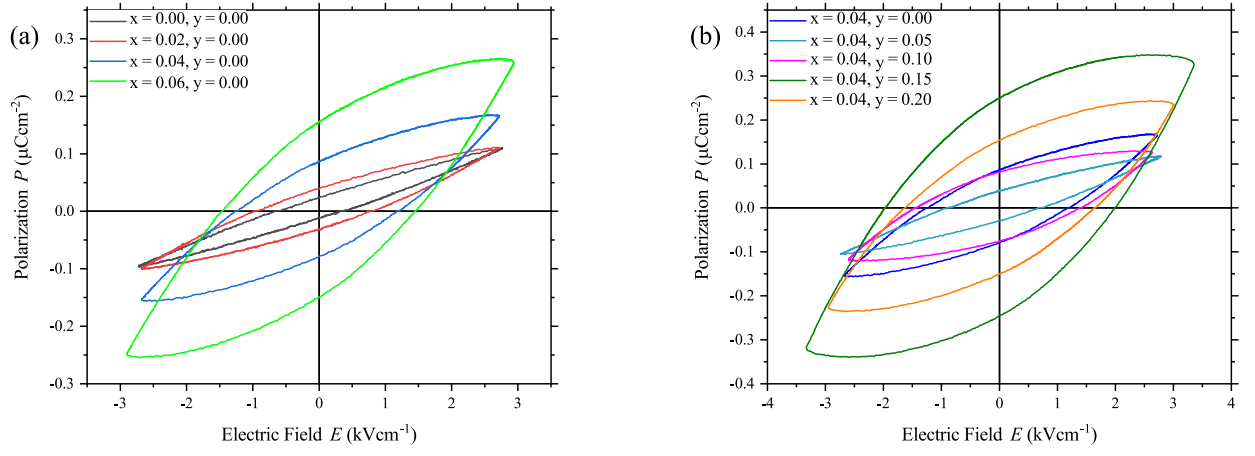


FIG. 10. P - E hysteresis loops of (a) $\text{Sr}_{1-x}\text{Zr}_x\text{TiO}_3$ for $x = 0.0, 0.02, 0.04$ and 0.06 , (b) $\text{Sr}_{0.96}\text{Zr}_{0.04}\text{Ti}_{1-y}\text{Ni}_y\text{O}_3$ with $y = 0.00, 0.05, 0.10, 0.15$ and 0.20 .

saturation, see Fig. 10(a). At $E = 3 \text{ kVcm}^{-1}$ the sample showed a $P_{\text{max}} = 0.103 \mu\text{Ccm}^{-2}$, a tiny $P_r = 0.017 \mu\text{Ccm}^{-2}$ and $E_c = 0.154 \text{ kVcm}^{-1}$. The incorporation of Zr seems to enhance FE behaviour in STO. For Zr doped $\text{Sr}_{1-x}\text{Zr}_x\text{TiO}_3$ samples, the P_r and E_c values monotonically increase with the Zr concentration, see Table II. For (Zr, Ni) co-doped $\text{Sr}_{0.96}\text{Zr}_{0.04}\text{Ti}_{1-y}\text{Ni}_y\text{O}_3$ sample with a composition of $y=0.05$, the Ni dopants diminish the ferroelectric characteristics by narrowing down the P - E loop ($E_c = 0.791 \text{ kVcm}^{-1}$, $P_r = 0.039 \mu\text{Ccm}^{-2}$ and $P_{\text{max}} = 0.112 \mu\text{Ccm}^{-2}$) as compared to $\text{Sr}_{0.96}\text{Zr}_{0.04}\text{TiO}_3$ ($E_c = 1.216 \text{ kVcm}^{-1}$, $P_r = 0.083 \mu\text{Ccm}^{-2}$ and $P_{\text{max}} = 0.162 \mu\text{Ccm}^{-2}$), see Fig. 10(b). The FE hysteresis existed for all (Zr, Ni) co-doped samples even for higher Ni concentrations; for example in case of $\text{Sr}_{0.96}\text{Zr}_{0.04}\text{Ti}_{0.90}\text{Ni}_{0.10}\text{O}_3$ sample $E_c = 1.420 \text{ kVcm}^{-1}$, $P_r = 0.079 \mu\text{Ccm}^{-2}$ and $P_{\text{max}} = 0.125 \mu\text{Ccm}^{-2}$. For higher doping concentration in Zr and (Zr, Ni) co-doped samples, the area of the PE loop was enlarged which indicates increased dielectric losses were present inside the sample. This is consistent with the increased leakage current in the samples as displayed in Table II. The origin of the leakage current can be due to carriers originated from the oxygen vacancies [65]. The dominance of the leakage current prevented complete saturation in polarization to occur in our samples [66].

H. Magnetization Measurements

We have recorded magnetization (M) vs. magnetic field (H) hysteresis loops of the as-prepared samples using a vibrating sample magnetometer applying a maximum magnetic field of $\pm 20 \text{ kOe}$ and displayed in Fig. 11. The inset of Fig. 11 shows an enlarged view of the hysteresis loop for the 4 % Zr and 10 % Ni co-doped $\text{Sr}_{0.96}\text{Zr}_{0.04}\text{Ti}_{0.90}\text{Ni}_{0.10}\text{O}_3$ sample. We extracted different M - H loop parameters such as remnant magnetiza-

P-E Hysteresis Loop Parameters					
x	y	E_c (kVcm^{-1})	P_r (μCcm^{-2})	P_{max} (μCcm^{-2})	I_d (μAcm^{-2})
0.00	0.00	0.312	0.011	0.103	0.073
0.02	0.00	0.768	0.032	0.106	0.076
0.04	0.00	1.216	0.083	0.162	0.085
0.06	0.00	1.458	0.153	0.260	0.108
0.04	0.05	0.791	0.039	0.112	0.077
0.04	0.10	1.420	0.079	0.125	0.083
0.04	0.15	1.983	0.247	0.344	0.136
0.04	0.20	1.632	0.152	0.240	0.149

TABLE II. The coercive field (E_c), the remnant polarization (P_r), the maximum polarization (P_{max}) and leakage current I_d at P_{max} of $\text{Sr}_{1-x}\text{Zr}_x\text{Ti}_{1-y}\text{Ni}_y\text{O}_3$ for different values of x and y .

tion (M_r), the coercive field (H_c) and the saturation magnetization (M_s); and the values were inserted in Table III. The H_c was quantified following the formula $H_c = (H_{c1} - H_{c2})/2$ where H_{c1} and H_{c2} are the left and right coercive fields respectively [67].

M-H Hysteresis Loop Parameters				
x	y	$M_r \times 10^{-3}$ (emu g^{-1})	H_c (Oe)	M_s (emu g^{-1})
0.00	0.00	35	4	2.80
0.04	0.00	64	92	0.50
0.04	0.05	114	60	1.30
0.04	0.10	322	375	1.27
0.04	0.15	246	371	1.00
0.04	0.20	365	308	0.50

TABLE III. The remnant magnetization (M_r), the coercive field (H_c) and the saturation magnetization (M_s) of $\text{Sr}_{1-x}\text{Zr}_x\text{Ti}_{1-y}\text{Ni}_y\text{O}_3$ for different values of x and y .

The saturated hysteresis loop with a saturation magnetization M_s of 2.80 emu g^{-1} and coercive field of 4 Oe

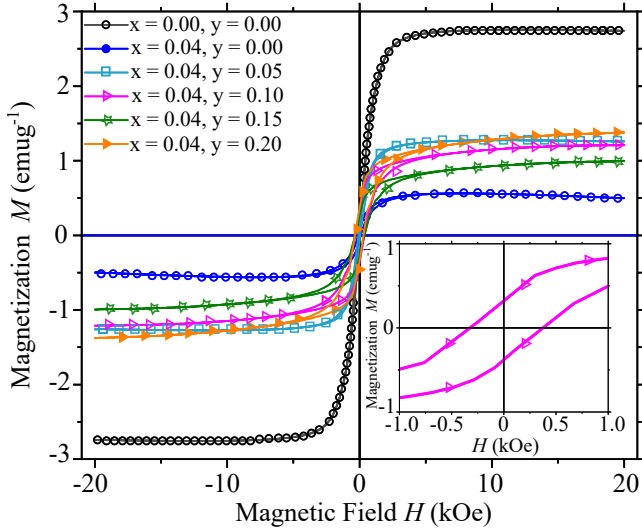


FIG. 11. Magnetic hysteresis loop of $\text{Sr}_{1-x}\text{Zr}_x\text{Ti}_{1-y}\text{Ni}_y\text{O}_3$ samples using vibrating sample magnetometer for $(x, y) = (0.00, 0.00), (0.04, 0.00), (0.04, 0.05), (0.04, 0.10), (0.04, 0.15), (0.04, 0.20)$. Inset: The enlarged view of the hysteresis loop for 4% Zr and 10% Ni co-doped sample.

revealed soft FM nature of the as-synthesized STO sample. The origin of FM behaviour can be attributed to the presence oxygen vacancies V_{O}^{2-} induced as a result of charge imbalance due to loss of Sr^{2+} at high sintering temperature [68–73]. Moreover the variable oxidation state of Ti ($\text{Ti}^{4+} \rightleftharpoons \text{Ti}^{3+}$) in STO can also facilitate oxygen vacancy to maintain charge equilibrium. The reduction in M_s to 0.50 emu g^{-1} in case of 4% Zr doped $\text{Sr}_{0.96}\text{Zr}_{0.04}\text{TiO}_3$ sample can be ascribed to diamagnetic Zr^{4+} ion with its empty $4d$ orbitals [74]. In addition, the presence of Zr^{4+} in the grain boundaries may reduce the defects at the grain surfaces that can cause suppression in M_s [70]. Moreover we observed increments in M_r and H_c as compared to those of undoped STO which indicates reduction in softness of FM order due to Zr doping. The incorporation of Ni dopants notably increased H_c and M_r in (Zr, Ni) co-doped STO. In particular, for 4% Zr and 10% Ni co-doped sample, the values of H_c , M_r and M_s are mentionable. For a further increment of the amount of Ni to 15% and 20%, H_c and M_r do not change significantly, however, M_s reduced notably. Due to Zr and Ni co-doping in STO, the coercivity enhancement was very high compared to that of undoped STO which might have originated from the inflated exchange coupling between Ni^{2+} ions mediated by trapped electron in the oxygen vacancy [75, 76]. Note also the variation in H_c with doping concentration is not surprising as it depends on large number of factors defining the microstructure of the sample such as grain homogeneity, grain size distribution and domain wall pinning [77]. For the case of remnant magnetization M_r , we observed an order of magnitude enhancement in $\text{Sr}_{0.96}\text{Zr}_{0.04}\text{Ti}_{0.90}\text{Ni}_{0.10}\text{O}_3$ sample

($322 \times 10^{-3} \text{ emu g}^{-1}$) as compared to that of undoped STO ($35 \times 10^{-3} \text{ emu g}^{-1}$). Overall the presence of hysteresis loop and the remnant magnetization corroborates long range FM order in our (Zr, Ni) co-doped samples.

IV. CONCLUSION

Undoped, Zr doped and (Zr, Ni) co-doped SrTiO_3 samples were synthesized with varying degrees of doping concentrations and were characterized comprehensively using the appropriate techniques. We confirmed the cubic phase up to 4% Zr doping in STO from Rietveld analysis of the powder X-ray diffraction pattern. The substitution of 4% Zr instead of Sr in STO improved the morphological, electrical and magnetic properties. Therefore, Zr and Ni co-doped samples were prepared for this fixed % of Zr to improve further the electrical and magnetic properties of STO. Interestingly, 4% Zr and 10% Ni co-doped $\text{Sr}_{0.96}\text{Zr}_{0.04}\text{Ti}_{0.90}\text{Ni}_{0.10}\text{O}_3$ sample demonstrated ~ 1 and ~ 2 orders of magnitude enhancement in remnant magnetization and coercivity respectively at room temperature. Along with a clear ferroelectric hysteresis loop we observed also a ferromagnetic hysteresis loop for this co-doped sample. We may anticipate that simultaneous existence of ferromagnetic and ferroelectric phases in this as-synthesized (Zr, Ni) co-doped $\text{Sr}_{0.96}\text{Zr}_{0.04}\text{Ti}_{0.90}\text{Ni}_{0.10}\text{O}_3$ sample may open up the potentials as a multiferroic material for use in multifunctional applications.

ACKNOWLEDGMENTS

We gratefully acknowledge the support from Dr. Ish-tiaque M. Syed for providing access to high temperature sintering facility in Semiconductor Technology Research Center, University of Dhaka.

AUTHOR CONTRIBUTIONS

S.A. and A. K. M. S. H. F. contributed equally.

Competing interests: The authors declare no competing interests.

- [1] J. Robertson, Journal of Vacuum Science & Technology B: Microelectronics and Nanometer Structures Processing, Measurement, and Phenomena **18**, 1785 (2000).
- [2] D. V. Christensen, F. Trier, W. Niu, Y. Gan, Y. Zhang, T. S. Jespersen, Y. Chen, and N. Pryds, Adv. Mater. Interfaces **6**, 1900772 (2019).
- [3] A. Eriksson, A. Deleniv, and S. Gevorgian, Journal of Applied Physics **93**, 2848 (2003).
- [4] D. Fuchs, C. W. Schneider, R. Schneider, and H. Ritschel, Journal of Applied Physics **85**, 7362 (1999).
- [5] K. Szot, W. Speier, G. Bihlmayer, and R. Waser, Nature Materials **5**, 312 (2006).
- [6] Y. Hu, O. K. Tan, J. S. Pan, and X. Yao, The Journal of Physical Chemistry B **108**, 11214 (2004).
- [7] D. D. Kajale, G. E. Patil, V. B. Gaikwad, S. D. Shinde, D. N. Chavan, N. K. Pawar, S. R. Shirsath, and G. H. Jain, International Journal on Smart Sensing & Intelligent Systems **5** (2012).
- [8] Y. Sakata, Y. Miyoshi, T. Maeda, K. Ishikiriya, Y. Yamazaki, H. Imamura, Y. Ham, T. Hisatomi, J. Kubota, A. Yamakata, *et al.*, Applied Catalysis A: General **521**, 227 (2016).
- [9] C. Li, K. C. K. Soh, and P. Wu, Journal of Alloys and Compounds **372**, 40 (2004).
- [10] N. A. Spaldin and R. Ramesh, Nature materials **18**, 203 (2019).
- [11] S. Kustov, I. Liubimova, and E. K. H. Salje, Physical Review Letters **124**, 016801 (2020).
- [12] K. A. Müller and H. Burkard, Physical Review B **19**, 3593 (1979).
- [13] J. Haeni, P. Irvin, W. Chang, R. Uecker, P. Reiche, Y. Li, S. Choudhury, W. Tian, M. Hawley, B. Craigo, *et al.*, Nature **430**, 758 (2004).
- [14] D. Choudhury, S. Mukherjee, P. Mandal, A. Sundaresan, U. Waghmare, S. Bhattacharjee, R. Mathieu, P. Lazor, O. Eriksson, B. Sanyal, *et al.*, Physical Review B **84**, 125124 (2011).
- [15] D. Yao, X. Zhou, and S. Ge, Applied Surface Science **257**, 9233 (2011).
- [16] A. J. Ahmed, S. M. K. Nazrul Islam, R. Hossain, J. Kim, M. Kim, M. Billah, M. S. A. Hossain, Y. Yamauchi, and X. Wang, Royal Society Open Science **6**, 190870 (2019).
- [17] E. Padmini and K. Ramachandran, Solid State Communications **302**, 113716 (2019).
- [18] M. Muralidharan, V. Anbarasu, A. E. Perumal, and K. Sivakumar, Journal of Materials Science: Materials in Electronics **25**, 4078 (2014).
- [19] D. Norton, N. Theodoropoulou, A. Hebard, J. Budai, L. Boatner, S. Pearton, and R. Wilson, Electrochemical and Solid State Letters **6**, G19 (2002).
- [20] J. Lee, Z. Khim, Y. Park, D. Norton, N. Theodoropoulou, A. Hebard, J. Budai, L. Boatner, S. Pearton, and R. Wilson, Solid-State Electronics **47**, 2225 (2003).
- [21] A. Durán, E. Martínez, J. Díaz, and J. Siqueiros, Journal of Applied Physics **97**, 104109 (2005).
- [22] A. Tkach, P. M. Vilarinho, and A. L. Kholkin, Acta Materialia **53**, 5061 (2005).
- [23] D. Choudhury, B. Pal, A. Sharma, S. Bhat, and D. D. Sarma, Scientific Reports **3**, 1433 (2013).
- [24] C. Azzoni, M. Mozzati, A. Paleari, V. Massarotti, M. Bini, and D. Capsoni, Solid State Communications **114**, 617 (2000).
- [25] M. Savinov, V. Trepakov, P. Syrnikov, V. Železný, J. Pokorný, A. Dejneka, L. Jastrabik, and P. Galinetto, Journal of Physics: Condensed Matter **20**, 095221 (2008).
- [26] H. S. Bhatti, S. T. Hussain, F. A. Khan, and S. Hussain, Applied Surface Science **367**, 291 (2016).
- [27] K. C. Pitike, W. D. Parker, L. Louis, and S. M. Nakhmanson, Physical Review B **91**, 035112 (2015).
- [28] W. Bian, X. Lu, Y. Li, C. Min, H. Zhu, Z. Fu, and Q. Zhang, Journal of Materials Science: Materials in Electronics **29**, 2743 (2018).
- [29] B. Ahmmad, M. Z. Islam, A. Billah, and M. A. Basith, Journal of Physics D: Applied Physics **49**, 095001 (2016).
- [30] M. A. Basith, A. Billah, M. A. Jalil, N. Yesmin, M. A. Sakib, E. K. Ashik, S. M. E. H. Yousuf, S. S. Chowdhury, M. S. Hossain, S. H. Firoz, and B. Ahmmad, Journal of Alloys and Compounds **694**, 792 (2017).
- [31] B. Soni, S. Makkar, and S. Biswas, Materials Characterization **174**, 110990 (2021).
- [32] W. Zhou, H. Deng, N. Ding, L. Yu, F. Yue, P. Yang, and J. Chu, Materials Characterization **107**, 1 (2015).
- [33] I. N. Esha, K. N. Munny, M. N. I. Khan, and K. H. Maria, AIP Advances **10**, 125026 (2020).
- [34] M. A. Basith, O. Kurni, M. S. Alam, B. L. Sinha, and B. Ahmmad, Journal of Applied Physics **115**, 024102 (2014).
- [35] G. Saravanan, K. Ramachandran, J. Gajendiran, and E. Padmini, Chemical Physics Letters, 137314 (2020).
- [36] H. Qiao, Z. Wei, H. Yang, L. Zhu, and X. Yan, Journal of Nanomaterials **2009** (2009).
- [37] B. D. Cullity, *Elements of X-ray Diffraction* (Addison-Wesley Publishing, 1956).
- [38] V.-I. Merupo, S. Velumani, K. Ordon, N. Errien, J. Szade, and A.-H. Kassiba, CrystEngComm **17**, 3366 (2015).
- [39] S. K. Rout, S. Panigrahi, and J. Bera, Bulletin of Materials Science **28**, 275 (2005).
- [40] P. S. Narayanan and K. Vedam, Zeitschrift für Physik **163**, 158 (1961).
- [41] W. G. Nilsen and J. G. Skinner, The Journal of Chemical Physics **48**, 2240 (1968).
- [42] R. F. Schaufele and M. J. Weber, The Journal of Chemical Physics **46**, 2859 (1967).
- [43] C. H. Perry, J. H. Fertel, and T. F. McNelly, The Journal of Chemical Physics **47**, 1619 (1967).
- [44] A. A. Sirenko, I. A. Akimov, J. R. Fox, A. M. Clark, H.-C. Li, W. Si, and X. X. Xi, Physical review letters **82**, 4500 (1999).
- [45] F. A. Rabuffetti, H.-S. Kim, J. A. Enterkin, Y. Wang, C. H. Lanier, L. D. Marks, K. R. Poepfelmeier, and P. C. Stair, Chemistry of Materials **20**, 5628 (2008).
- [46] D. A. Tenne, I. E. Gonenli, A. Soukiassian, D. G. Schlom, S. M. Nakhmanson, K. M. Rabe, and X. X. Xi, Physical Review B **76**, 024303 (2007).
- [47] T. Xian, H. Yang, L. Di, J. Ma, H. Zhang, and J. Dai, Nanoscale Research Letters **9**, 1 (2014).
- [48] C. Srilakshmi, R. Saraf, and C. Shivakumara, ACS Omega **3**, 10503 (2018).
- [49] S. K. Patil, N. Shah, F. D. Blum, and M. N. Rahaman, Journal of Materials Research **20**, 3312 (2005).
- [50] T. Xie, Y. Wang, C. Liu, and L. Xu, Materials **11**, 646

- (2018).
- [51] P. Ganguly, A. Jha, and K. Deori, Solid State Communications **146**, 472 (2008).
 - [52] Priyanka and A. Jha, Bulletin of Materials Science **36**, 135 (2013).
 - [53] S. O. Kasap, *Principles of Electronic Materials and Devices* (Tata McGraw-Hill, 2006).
 - [54] A. Hossain, I. N. Esha, I. B. Elius, M. N. I. Khan, and K. H. Maria, Journal of Materials Science: Materials in Electronics, **1** (2020).
 - [55] M. Muralidharan, V. Anbarasu, A. E. Perumal, and K. Sivakumar, Journal of Materials Science: Materials in Electronics **26**, 6352 (2015).
 - [56] J. Qi, M. Cao, Y. Chen, Y. Fang, W. Pan, H. Hao, Z. Yao, Z. Yu, and H. Liu, Journal of Alloys and Compounds **762**, 950 (2018).
 - [57] M. S. Fu, X. Q. Liu, and X. M. Chen, Journal of the European Ceramic Society **28**, 585 (2008).
 - [58] E. R. Kipkoech, F. Azough, and R. Freer, Journal of Applied Physics **97**, 064103 (2005).
 - [59] A. Dutta, T. P. Sinha, and S. Shannigrahi, Physical Review B **76**, 155113 (2007).
 - [60] H. Trabelsi, M. Bejar, E. Dhahri, M. Sajieddine, K. Khirouni, P. R. Prezias, B. M. G. Melo, M. A. Valente, and M. P. F. Graça, Journal of Alloys and Compounds **723**, 894 (2017).
 - [61] M. Smari, H. Rahmouni, N. Elghoul, I. Walha, E. Dhahri, and K. Khirouni, RSC Advances **5**, 2177 (2014).
 - [62] J. R. Jurado, M. T. Colomer, and J. R. Frade, Journal of the American Ceramic Society **83**, 2715 (2000).
 - [63] M. Vollman and R. Waser, Journal of the American Ceramic Society **77**, 235 (1994).
 - [64] M. Vollmann, R. Hagenbeck, and R. Waser, Journal of the American Ceramic Society **80**, 2301 (1997).
 - [65] T. Shibata, S. Chattopadhyay, B. Lin, and V. R. Palkar, in *AIP Conference Proceedings*, Vol. 882 (American Institute of Physics, 2007) pp. 780–782.
 - [66] S. S. Chowdhury, A. H. M. Kamal, R. Hossain, M. Hasan, M. F. Islam, B. Ahmmad, and M. A. Basith, Ceramics International **43**, 9191 (2017).
 - [67] M. A. Basith, F. A. Khan, B. Ahmmad, S. Kubota, F. Hirose, D.-T. Ngo, Q.-H. Tran, and K. Mølhave, Journal of Applied Physics **118**, 023901 (2015).
 - [68] W. Xu, J. Yang, W. Bai, K. Tang, Y. Zhang, and X. Tang, Journal of Applied Physics **114**, 154106 (2013).
 - [69] K. C. Verma, R. K. Kotnala, N. Thakur, V. S. Rangra, and N. S. Negi, Journal of Applied Physics **104**, 093908 (2008).
 - [70] Z. Zhang, J. Hu, Z. Xu, H. Qin, L. Sun, F. Gao, Y. Zhang, and M. Jiang, Solid State Sciences **13**, 1391 (2011).
 - [71] D. A. Crandles, B. DesRoches, and F. S. Razavi, Journal of Applied Physics **108**, 053908 (2010).
 - [72] K. Potzger, J. Osten, A. A. Levin, A. Shalimov, G. Talut, H. Reuther, S. Arpacı, D. Bürger, H. Schmidt, T. Nestler, *et al.*, Journal of Magnetism and Magnetic materials **323**, 1551 (2011).
 - [73] S. Middey, C. Meneghini, and S. Ray, Applied Physics Letters **101**, 042406 (2012).
 - [74] S. H. Blundell, *Magnetism in Condensed Matter*, 1st ed. (Oxford. Univ. Press Inc., 2001).
 - [75] Z. Ren, G. Xu, X. Wei, Y. Liu, X. Hou, P. Du, W. Weng, G. Shen, and G. Han, Applied Physics Letters **91**, 063106 (2007).
 - [76] S. Lei, L. Liu, C. Wang, X. Shen, D. Guo, C. Wang, S. Zeng, B. Cheng, Y. Xiao, and L. Zhou, CrystEngComm **16**, 1322 (2014).
 - [77] B. Ahmmad, K. Kanomata, K. Koike, S. Kubota, H. Kato, F. Hirose, A. Billah, M. A. Jalil, and M. A. Basith, Journal of Physics D: Applied Physics **49**, 265003 (2016).

Supplementary information for
“Room temperature ferroic orders in Zr and (Zr, Ni)
doped SrTiO₃”

Shahran Ahmed,¹ A. K. M. Sarwar Hossain Faysal,¹ M. N. I. Khan,^{2,*} M. A. Basith,^{3,†}
Muhammad Shahriar Bashar,⁴ H. N. Das,² Tarique Hasan,¹ and Imtiaz Ahmed^{1,‡}

¹*Department of Electrical and Electronic Engineering,
University of Dhaka, Dhaka-1000, Bangladesh*

²*Materials Science Division, Atomic Energy Centre, Dhaka-1000, Bangladesh*

³*Nanotechnology Research Laboratory, Department of Physics,
Bangladesh University of Engineering and Technology, Dhaka-1000, Bangladesh*

⁴*Institute of Fuel Research and Development,
Bangladesh Council of Scientific and Industrial Research, Dhaka-1205, Bangladesh*

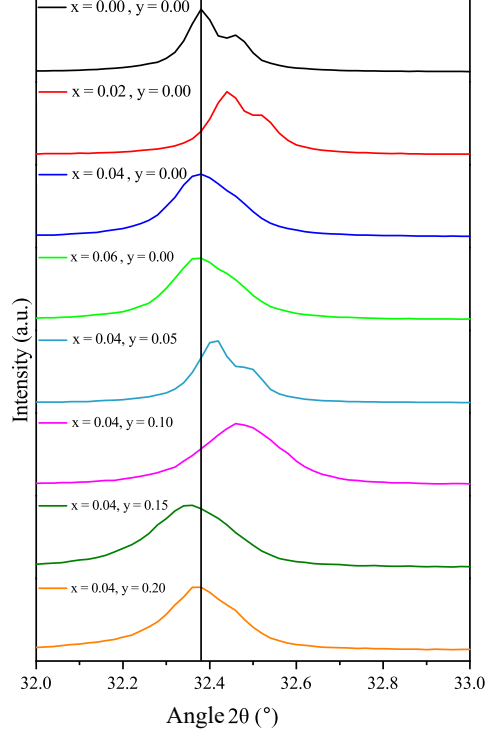


FIG. S1. The evolution of XRD intensity peak of (110) plane of $\text{Sr}_{1-x}\text{Zr}_x\text{Ti}_{1-y}\text{Ni}_y\text{O}_3$ for $(x, y) = (0.00, 0.00), (0.02, 0.00), (0.04, 0.00), (0.06, 0.00), (0.04, 0.05), (0.04, 0.10), (0.04, 0.15)$ and $(0.04, 0.20)$.

XRD PEAK EVOLUTION

The highest intensity peak (110) shifts as Zr and Ni dopants are introduced in the sample, see Fig. S1. These shifts can be attributed to strains induced in the STO cubic structure due to the incorporation of Zr and Ni. Peak shift towards lower diffraction angle usually results from tensile strain due to dopant ions with smaller radii Zr^{4+} ($r_o = 0.80 \text{ \AA}$) replacing the Sr^{2+} ($r_o = 1.26 \text{ \AA}$) in A-site; or Ni^{2+} ($r_o = 0.69 \text{ \AA}$) replacing Ti^{4+} ($r_o = 0.74 \text{ \AA}$) in B-site. Peak shift towards higher angle results from compressive strain; for example the bigger Zr^{4+} ($r_o = 0.80 \text{ \AA}$) ion replacing smaller Ti^{4+} ($r_o = 0.74 \text{ \AA}$). At low Zr concentration such as $x=0.02$, the XRD peak shifted to higher angle indicating the presence of a compressive strain as some of the Zr^{4+} ions may have substituted the Ti^{4+} . But as the Zr concentration was increased to 4% and 6%, the peak moved to lower diffraction angle as more Zr^{4+} ions started

to substitute Sr^{2+} . It is evident the peak shift between pure STO and $\text{Sr}_{0.96}\text{Ni}_{0.04}\text{TiO}_3$ is very nominal almost conforming with pure cubic phase. The changes in the full-width-at-half-maximum (FWHM) for (Zr, Ni) co-doped samples indicates slight distortion and disorder due to size differences of substituted dopants and possible interstitial dopants respectively.

RIETVELD REFINEMENT

Rietveld refined analysis for Wyckoff position, bond lengths and bond angles														
<u>SrTiO₃</u>					<u>Sr_{0.96}Zr_{0.04}TiO₃</u>					<u>Sr_{0.96}Zr_{0.04}Ti_{0.90}Ni_{0.10}O₃</u>				
atom	site	x _w	y _w	z _w	atom	site	x _w	y _w	z _w	atom	site	x _w	y _w	z _w
Sr	1a	0	0	0	Sr	1a	0.0	0.0	0.0	Sr	1a	0.0	0.0	0.0
Ti	1b	0.5	0.5	0.5	Ti	1b	0.5	0.5	0.5	Ti	1b	0.5	0.5	0.5
O	3c	0.0	0.5	0.5	O	3c	0.0	0.5	0.5	O	3c	0.0	0.5	0.5
					Zr	1a	0.0	0.0	0.0	Zr	1a	0.0	0.0	0.0
										Ni	1b	0.5	0.5	0.5
<u>Bond length (Å)</u>					<u>Bond length (Å)</u>					<u>Bond length (Å)</u>				
Ti-O		1.953 (3)			Ti-O		1.955 (5)			Ti/Ni-O		1.957 (6)		
Sr-O		2.762 (4)			Sr/Zr-O		2.762 (4)			Sr/Zr-O		2.768 (8)		
<u>Bond angle (°)</u>					<u>Bond angle (°)</u>					<u>Bond angle (°)</u>				
⟨Sr-O-Sr⟩		90, 180			⟨Sr/Zr-O-Sr/Zr⟩		90, 180			⟨Sr/Zr-O-Sr/Zr⟩		90, 180		
⟨Sr-O-Ti⟩		90			⟨Sr/Zr-O-Ti⟩		90			⟨Sr/Zr-O-Ti/Ni⟩		90		
R _p		5.755			R _p		5.334			R _p		5.462		
R _{wp}		7.580			R _{wp}		7.169			R _{wp}		7.32		
R _{exp}		2.023			R _{exp}		1.997			R _{exp}		1.923		
χ ²		3.748			χ ²		3.590			χ ²		3.806		

TABLE S1. Atomic coordinates x_w , y_w , z_w in Wyckoff notation, bond lengths and bond angles obtained from Rietveld refinement of XRD patterns of SrTiO_3 , $\text{Sr}_{0.96}\text{Zr}_{0.04}\text{TiO}_3$ and $\text{Sr}_{0.96}\text{Zr}_{0.04}\text{Ti}_{0.90}\text{Ni}_{0.10}\text{O}_3$.

EDX PEAK ANALYSIS

To perform chemical species identification of our samples Energy-dispersive X-ray spectroscopy (EDX) spectra for SrTiO_3 , $\text{Sr}_{0.96}\text{Zr}_{0.04}\text{TiO}_3$ and $\text{Sr}_{0.96}\text{Zr}_{0.04}\text{Ti}_{0.90}\text{Ni}_{0.10}\text{O}_3$ samples have been obtained as shown in Fig. S2. The atomic weights (%) of chemical species obtained from EDX measurements were compared with corresponding theoretical values for all aforementioned samples, see Table S2.

EDX Analysis			
	Element	EDX Atomic (%)	Theoretical Atomic (%)
SrTiO_3	Sr	15.54	20
	Ti	19.98	20
	O	64.57	60
$\text{Sr}_{0.96}\text{Zr}_{0.04}\text{TiO}_3$	Sr	16.12	19.2
	Ti	23.96	20
	O	59.25	60
	Zr	0.67	0.8
$\text{Sr}_{0.96}\text{Zr}_{0.04}\text{Ti}_{0.90}\text{Ni}_{0.10}\text{O}_3$	Sr	16.58	19.2
	Ti	20.82	18
	O	57.36	60
	Zr	0.54	0.8
	Ni	4.7	2

TABLE S2. Chemical species identification and concentration analysis using EDX of SrTiO_3 , $\text{Sr}_{0.96}\text{Zr}_{0.04}\text{TiO}_3$ and $\text{Sr}_{0.96}\text{Zr}_{0.04}\text{Ti}_{0.90}\text{Ni}_{0.10}\text{O}_3$ samples.

Raman Peak Assignment

The Raman peaks for SrTiO_3 , $\text{Sr}_{0.96}\text{Zr}_{0.04}\text{TiO}_3$ and $\text{Sr}_{0.96}\text{Zr}_{0.04}\text{Ti}_{0.9}\text{Ni}_{0.1}\text{O}_3$ samples were identified with their transverse acoustic (TA), longitudinal acoustic (LA), transverse optical (TO) and longitudinal optical (LO) vibrational phonon modes in Table S3.

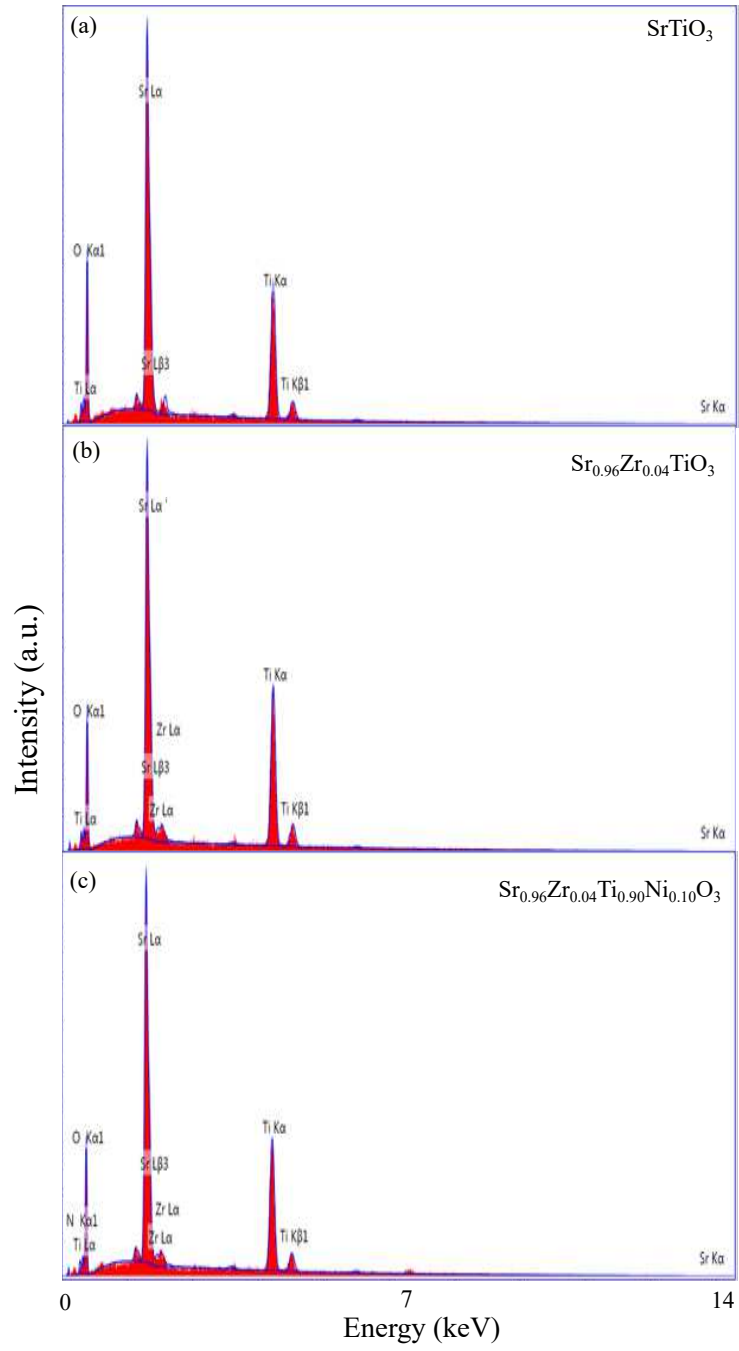


FIG. S2. EDX spectra of (a) SrTiO_3 , (b) $\text{Sr}_{0.96}\text{Zr}_{0.04}\text{TiO}_3$ and (c) $\text{Sr}_{0.96}\text{Zr}_{0.04}\text{Ti}_{0.90}\text{Ni}_{0.10}\text{O}_3$.

Raman Peak Analysis			
Peak	SrTiO ₃	Sr _{0.96} Zr _{0.04} TiO ₃	Sr _{0.96} Zr _{0.04} Ti _{0.90} Ni _{0.10} O ₃
Assgn.	(cm ⁻¹)	(cm ⁻¹)	(cm ⁻¹)
TO ₁	148	160	145
2TA	208	201	202
TO ₁ +LA	275	285	274
LO ₁ +TA,	383	377	374
2TO ₂			
TO ₄	547	-	-
TO ₁ +TO ₄	-	641	-
LA+LO ₃	702	701	689
LO ₃ +TO ₂	-	-	762
LO ₄	797	800	-

TABLE S3. Experimentally observed Raman peak assignments to different phonon vibrational modes of SrTiO₃, Sr_{0.96}Zr_{0.04}TiO₃ and Sr_{0.96}Zr_{0.04}Ti_{0.90}Ni_{0.10}O₃.

Fourier Transform Infrared Spectroscopy (FTIR)

The FTIR absorption peaks for SrTiO₃, Sr_{0.96}Zr_{0.04}TiO₃ and Sr_{0.96}Zr_{0.04}Ti_{0.90}Ni_{0.10}O₃ were identified with their chemical bonds vibrations inside the samples in Table S4.

FTIR Absorption Peak Analysis			
Peak	SrTiO ₃	Sr _{0.96} Zr _{0.04} TiO ₃	Sr _{0.96} Zr _{0.04} Ti _{0.90} Ni _{0.10} O ₃
Assignment	(cm ⁻¹)	(cm ⁻¹)	(cm ⁻¹)
TiO ₂	366	366	370
TiO ₆	598	594	536
C-OH	1462	1460	1485
-OH	1653	1652	-
-OH	3465	3465	-

TABLE S4. Experimentally observed FTIR absorption peak assignment to different chemical bond vibrational modes of SrTiO₃, Sr_{0.96}Zr_{0.04}TiO₃ and Sr_{0.96}Zr_{0.04}Ti_{0.90}Ni_{0.10}O₃.

* `ni_khan77@yahoo.com`

† `mabasith@phy.buet.ac.bd`

‡ `imtiaz@du.ac.bd`